

Development of a Subsonic Sounding Rocket for Research Flights of Variable Payloads

A project present to
The Faculty of the Department of Aerospace Engineering
San Jose State University

in partial fulfillment of the requirements for the degree
Master of Science in Aerospace Engineering

By

Ted W. Bohrer

May, 2017

approved by

Dr. Periklis Papadopoulos
Faculty Advisor



c 2017

Ted W. Bohrer

ALL RIGHTS RESERVED

The Designated Thesis Committee Approves the Thesis Titled

DEVELOPMENT OF A SUBSONIC SOUNDING ROCKET FOR RESEARCH
FLIGHTS OF VARIABLE PAYLOADS

by

Ted W. Bohrer

APPROVED FOR THE DEPARTMENT OF AEROSPACE ENGINEERING

SAN JOSE STATE UNIVERSITY

May 2017

Dr. Periklis Papadopoulos Department of Aerospace Engineering

ABSTRACT

DEVELOPMENT OF A SUBSONIC SOUNDING ROCKET FOR RESEARCH FLIGHTS OF VARIABLE PAYLOADS

by Ted W. Bohrer

Project FIFI was an eight month design space exploration that resulted in the construction of a subsonic sounding rocket for aerodynamics research. The project began with acceptance into the annual NASA University Student Launch Initiative, which is a mission based challenge hosted by Marshall Space Flight Center. Unhindered by rare weather conditions that forced resignation from the competition, the project continued. While most of the original mission requirements were maintained, some were adapted to meet the need at SJSU for a subsonic research vehicle. A full engineering life-cycle was followed that included teleconferences with a panel of NASA engineers to present major design review milestones. Preliminary designs based on theory and computer simulation, were tested in a sub-scale prototype launch, that included a reaction wheel payload. Based on experimental results of the test launch, a full-scale design was finalized and constructed. With a modified scientific payload for skin friction research, the full-scale rocket was launched. Live telemetry of the maiden flight, confirmed nominal function of all subsystems and the design was validated by a successful recovery.

TABLE OF CONTENTS

CHAPTER

1	INTRODUCTION	2
2	BACKGROUND	4
2.1	Natural Stability	5
2.2	Telemetry	6
2.3	Drag Induction	7
3	PROJECT OBJECTIVE	10
4	METHODOLOGY	11
5	MISSION REQUIREMENTS	13
6	DESIGN	14
6.1	Materials	14
6.2	Airframe	17
6.2.1	Body	17
6.2.2	Nose	18
6.2.3	Stability	19
6.2.4	Summary	21
6.3	Propulsion	24
6.4	Recovery	28
6.4.1	Electronics Bay	28

6.4.2 Parachute	30
6.5 Payload	31
6.5.1 Reaction Wheel	31
6.5.2 Sensor Package	33
7 SIMULATION	37
7.1 Computational Fluid Dynamics (CFD)	37
7.2 Finite Element Analysis (FEA)	40
8 RESULTS	41
8.1 Sub-scale Flight	41
8.2 Fullscale Flight	44
9 DISCUSSION	47
10 CONCLUSION	50
11 FUTURE WORK	52
REFERENCES	53
APPENDIX	
A ARDUINO CODE	54
B ADDITIONAL SCHEMATICS	56

LIST OF TABLES

Table

6.1 Material properties for 4 in. diameter tubes	14
6.2 Epoxy properties	16
6.3 Weight of G-12 at various lengths and diameters	17

LIST OF FIGURES

Figure

6.1 Payload section identification	17
6.2 Drag characteristics of various nose cones	19
6.3 Barrowman	19
6.4 Old fin stability diagram	20
6.5 New fin stability diagram	21
6.6 Final airframe design	22
6.7 Final fin design	23
6.8 Cut-away of nose	23
6.9 Aerotech L1150R thrust curve	26
6.10 Flight simulation plot	27
6.11 Electronics bay	29
6.12 Flight computer wiring	30
6.13 72" Iris Ultra descent vs weight	31
6.14 Reaction wheel assembly	32
6.15 Reaction system placement	32
6.16 Simulink controller design	33
6.17 Wheatstone bridge circuit	35
7.1 Computational mesh	37
7.2 Control volume	38
7.3 Velocity profile	39

7.4	Pressure profile	39
7.5	Structural analysis of airframe	40
7.6	Close-up of stress region	40
8.1	Sub-scale telemetry - launch pad	41
8.2	Sub-scale telemetry - ascent	42
8.3	Sub-scale telemetry - descent	42
8.4	Sub-scale telemetry - landing	43
8.5	Sub-scale telemetry - summary	43
8.6	Full-scale telemetry - launch pad	44
8.7	Full-scale telemetry - ascent	45
8.8	Full-scale telemetry - descent	45
8.9	Full-scale telemetry - landing	46
8.10	Full-scale telemetry - summary	46
B.1	Arduino Uno schematic	56
B.2	Adafruit 10 DOF IMU schematic	56
B.3	Adafruit SD reader schematic	57
B.4	Arduino to SD reader wiring	57

Nomenclature

C_d Coefficient of Drag

C_g Center of Gravity

C_p Center of Pressure

DOF Degree of Freedom

ESC Electronic Speed Controller

IMU Inertial Measurement Unit

R Resistance

rpm Revolutions per Minute

V Voltage

CHAPTER 1

INTRODUCTION

Project FIFI began as a competition rocket for the NASA University Student Launch Initiative (USLI), an annual challenge where hundreds of students compete nationally to meet technically demanding launch vehicle requirements. As described by NASA, USLI is a research-based, competitive, and experimental exploration project that provides relevant and cost effective research and development. The university level contest involves an intensive 8-month commitment to design, build, and launch a sophisticated, high-power rocket that supports NASA research and mission objectives.[1] For those that are more familiar with aircraft, USLI is the rocketry equivalent of Design Build Fly (DBF). The challenge for 2017 was to design, build, and launch a high-powered rocket that satisfied two mission objectives while being constrained to a strict set of parameters. The first objective was to fly to a target altitude of exactly one mile with as little deviation as possible. In fact, a deviation above 6% warranted disqualification from altitude scoring. Secondly, the rocket was to have a scientific payload section which would fly one of three payloads designed by the team to satisfy specific NASA mission objectives. Choice objectives included: post-burnout longitudinal axis control (roll maneuver), target acquisition with vertical landing, and fragile payload protection. The roll maneuver is to initiate at least two spins around the longitudinal axis during un-powered ascent and then steady for the remainder of flight to apogee. The target acquisition system is to correctly identify colored targets on the ground before descending to a vertical landing. Finally, the fragile payload protection is the safe launch and return of an

unknown quantity of mystery items, where only the maximum volume is known. From these options, Project FIFI focused on the roll maneuver because it was the most directly related to aerospace research.

The target altitude challenge was more difficult than expected due to the limitation on forward thrust. Since forward thrust was expressly forbidden, the target altitude needed to be met by careful use of the equations of motion. By combining atmospheric prediction, design space exploration, and computer simulation, a vehicle design was created that has the optimal balance of weight, aerodynamics, and propulsion necessary for the target altitude without forward thrust.

Following a rigorous proposal selection and acceptance, Project FIFI competed in a series of design reviews that mirrored the NASA engineering life cycle. Unfortunately, towards the end of the eight month competition, the west coast was hit with major storms that prevented meeting a critical test launch deadline. By missing the milestone, Project FIFI was forced to officially resign from the competition, though in actuality, continued to see the project to completion with only slight modification. The second mission objective, scientific payload, was modified to include a 4th choice by request of the SJSU AE department. Since the rocket no longer was competing in the NASA competition, an array of sensors for aerodynamics research was of greater benefit for future students, than the originally chosen roll maneuver.

For completeness, both the original roll maneuver payload and substituted sensor package are presented, but the focus of work discussed is in the launch vehicle creation and associated design space exploration.

CHAPTER 2

BACKGROUND

As this project was an entire working rocket system, with a complex set of functioning subsystems, key technologies from several disciplines were researched and incorporated. Of the subsystems, and particularly one of the payload options, the most difficult was potentially the roll maneuver during un-powered ascent. This was especially difficult because the roll had to be carried out through mechanical means only due to the launch vehicle restriction on thrusters, forward canards, and inherent geometry that passively induces the spin. All of these limitations lead to the implementation of a reaction wheel for longitudinal control, similar to the ones used on small satellites for attitude control. The other payload option, sensors for skin friction drag assessment, requires research into methods of measurement. Even though modeling and experimental data can reasonably predict apogee, the vehicle may need a way to induce drag to prevent overshooting the altitude ceiling and so these were also investigated. Much research is being conducted on air brake systems for re-entry vehicles and even though most are designed for supersonic to hypersonic flight conditions, the technology may still be beneficial for subsonic application as well. To prevent overshooting the target altitude, conduct the roll maneuver and regain longitudinal stability for the remainder of ascent, research into feedback control systems is needed. Since the competition has motor restrictions and specific vehicle velocity minimums and maximums at different stages of the flight, motor research is appropriate. Additionally, the motor restriction coupled with stability requirements means that the airframe and fins must be aerodynamically optimized

to result in low drag and an advantageous center of pressure. As part of the roll maneuver challenge, the rocket must be able to confirm successful longitudinal control. Although this data can be stored locally on-board the vehicle, the addition of a telemetry system can transmit this data for real time confirmation as well as provide useful recovery information such as decent rate, drift, and GPS coordinates.

2.1 Natural Stability

Prior to designing a control system for longitudinal attitude, the natural longitudinal stability was assessed. In a study conducted at NASA Langley Research Center, the effect of misaligned fins on longitudinal stability was investigated.[4] The report, "Statistical Analysis of the Roll Rate of a Launch Vehicle Under the Influence of Random Fin Misalignments" presented statistical methods for the predicted roll rate caused by misaligned fins. Asymmetries of the vehicle due to improper manufacture and uncertainties of measurement created a situation where the roll effect was a product of indeterminate quantity, and therefore amenable to statistical analysis. In a case where the desired roll rate was zero, the paper statistically showed that the uncertainty of misaligned fins caused a first-order effect. Since the researchers were only concerned with the zero roll rate case, no proof was provided to back the claim, that if a non-zero roll rate was desired, the effect of misaligned fins was usually considered second-order. The primary reason to understand these effects, was the catastrophic impact they can have on launch vehicles, especially those constructed without high precision equipment. Even when carefully constructed, the limitations of measurement almost guaranteed that there existed at least slight fin misalignment. Danger came when the roll rate became coincident with the pitch frequency and pitch-roll resonance

began to occur. This led to an undesirable precession and nutation that grew in amplitude, which in best case reduced the apogee altitude and worst case, structural failure and loss of the vehicle. Although a work of fiction, a great example of that scenario is described in “The Martian”, by Andy Weir.[3] A shift in the payload caused the rocket to begin a precession during ascent, that amplifies with resonance and ultimately caused complete structural failure. In all practicality, it is impossible to eliminate the natural roll during rocket flight but the design objective is to make it highly unlikely for there to be long periods of coincidence between roll and pitch frequencies. What makes the task harder, is that over the course of a flight, these frequencies naturally progress towards each other. Through mathematical derivation, Madden showed that a tolerance of misalignment can be determined, for a given fin configuration, that yielded a low probability of resonance.

2.2 Telemetry

As part of an STEM outreach program, AIAA-Wisconsin designed a prototype rocket as proof of concept for which a full-scale sounding rocket implantation could provide scientific payload launch services to students throughout the state.[2] Prior to construction, the team made an assessment of improvements the team could make towards rocketry. By using Pareto charts, which are based on Pareto Law, the team found that the most common launch failures recorded by the National Association of Rocketry at the Major Richard I. Bong experimental launch facility, were a result of parachute deployment and recovery system malfunctions.[2] When a failure occurred, cost to stakeholder increased in an attempt to recover data from on-board logging systems, which could be mitigated by a telemetry system. By having data from sensors transmitted back to a ground station, pre-failure

information was available to engineers to help the issue be assessed. For the purpose of creating a telemetry link, the AIAA-Wisconsin team used an AltusMetrum which contained several on-board sensors. Vehicle performance was tracked in real time with several multi-axis accelerometers, a barometric sensor to compute altitude and a global positioning chip for longitude and latitude determination. Telemetry was accomplished by packet radio communication on 70cm frequency band (also known as 440 MHz) between the AltusMetrum and a ground station computer equipped with an appropriate antenna. Usage of that band was regulated by the Federal Communications Commission (FCC) and required a licensed amateur radio operator (HAM). Similar telemetry setups existed in alternate flight computers that did not require an amateur radio license but those systems used a commercially issued FCC frequency and cost significantly more. In addition to the ground station being equipped with an antenna, data logging software, such as the one written by Keith Packard, interpreted the incoming packets. Vehicle performance was logged to disk and shown in real time while voice synthesis called out key audible updates that allowed viewers to keep their eyes on the rocket in the sky. GPS data can be imported to Google and overlaid on maps to visualize the entire flight and aid in recovery upon landing.

2.3 Drag Induction

Drag induction devices, also known as decelerators, were a common topic of research in spacecraft design. These devices were researched primarily to slow the entry of space vehicles into an atmosphere, such as the Mars Science Laboratory, and to de-orbit out of life satellites. Although the primary research in decelerators belonged to the supersonic and hypersonic regime, Sandia National Laboratories was

researching a solution to replace the subsonic parachute. In “The Development of a Ram Air Decelerator for the Recovery of Artillery Shells”[5], a method of drag induction was tested for atomic artillery shells, that no longer used a parachute. The issue, was that parachutes had shroud lines that could become tangled or damaged by the shell due to residual angular velocity as a result of the shells being spin stabilized. The proposed design, utilized a set of ram air ducts that, on descent, inflated a closed fabric container attached to the shell. There were two main advantages over parachutes. Since the container was fixed to the shell, any nutation experienced by the shell, was also experienced by the container, which eliminated contact damage. The inflated shell also helped to de-spin the shell through torsional air drag. Tests conducted in pressure chambers or other simulated environments without a spin, proved to be successful. In artillery testing, strength of materials became the failure point as the device was ripped from the shell by high centrifugal forces. Technion, Israel Institute of Technology, presented another subsonic decelerator device in “Deployable Conical Stabilizer and Decelerator”.[6] Intended as a low cost alternative to complex decelerator systems, the cone shaped device was inflated by a mechanical support structure. Analysis and tests confirmed that drag production of the device was limited by the strength of the supports used. Subjected to extremely low flow speeds, a spring-loaded collapsible ring was the best support. The ring allowed the cone to have a major diameter up to twice the diameter of the body it was released from, thus increased drag. However, the spring-loaded ring collapsed when subjected to Mach 0.3 flow. Better results were obtained for moderate subsonic flow when a rigid hem was used instead of the collapsible ring. Although the rigid support was able to withstand higher flow velocities, produced drag was less due to the major diameter being restricted to the deployment device. Other support structures were examined, such as ribs, but these

required more complex mechanical configurations and were deemed less cost effective. Research concluded that the collapsible spring was ideal for Mach 0.25 and below, between Mach 0.25 and 0.6, the rigid hem was better. Anything that exceeded Mach 0.6 was outside a low cost budget.

CHAPTER 3

PROJECT OBJECTIVE

The general objective of the project was to design, construct, and launch a fully functional launch vehicle that meets all the mission requirements outlined by NASA for the 2017 University Student Launch Initiative, with the exception of a different payload. These objectives were further broken down into levels of success, also known as success criteria.

Minimal - The design and creation of a fully functional high-powered rocket that meets the NASA mission requirements

Nominal - Safe flight and successful recovery

Complete - Acquisition of aerodynamics data from the experimental launch

CHAPTER 4

METHODOLOGY

In order to meet the specified objectives within eight months, the team followed the standard NASA engineering life cycle, which included a series of design reviews. These design reviews are extensive technical documents published to the public on a team maintained website. After each review was published, the team presented to a NASA engineering panel via teleconference, where each aspect of the design was evaluated and questioned for justification. Following proposal acceptance, the team had about one month to produce a Preliminary Design Review (PDR). During the PDR, the team presented several options for each element of the rocket design and explained the benefits and trade offs for each selection. During the couple months following the PRD, the team finalized the majority of design decisions and constructed a sub-scale prototype. After successfully launching the prototype, experimental data was utilized to finalize the launch vehicle design. The new improved design was presented at the second major review, known as the Critical Design Review (CDR). Using feedback from the NASA engineering panel and lessons learned from the prototype, the team began construction of the full-scale launch vehicle in preparation for the third major section of the engineering life-cycle. The Flight Readiness Review (FRR) was used to audit the entire system and confirm operational readiness overall, including ground hardware, software, personnel and procedures. With full-scale construction completed and successful analysis of all systems, the rocket was ready for the fourth major review, the Launch Readiness Review (LRR), which is conducted at the launch site by a panel

of certified rocket experts. During this review, the team presented the entire launch vehicle readied for flight except for energetic materials, and submitted to a detailed, deconstructive, hands-on inspection. In addition to vehicle inspection, the team demonstrated final flight readiness with previous launch data, an explanation of flight anomalies with appropriate mitigations, and a pre-flight check list. Following the final full-scale launch, the team gathered experimental data and prepared the results for the Post-Launch Assessment Review (PLAR).

CHAPTER 5

MISSION REQUIREMENTS

The primary source of mission requirements came from the restrictions listed in the University Student Launch Initiative Handbook[1], though some elements were modified to accommodate the new purpose of the rocket. By maintaining the majority of competition requirements, the project kept the real world challenges, much like those that would be seen within industry.

- Target altitude of exactly 1 mile
- Total impulse restricted to 5,120 Newton-Seconds
- Rail exit velocity at least 52 ft/sec
- Minimum static stability of 2.0
- Landing impact restricted to 150 ft-lbf
- Velocity does not exceed Mach 1 at any point
- Electronically track each separable section

CHAPTER 6

DESIGN

The design presented here, is intended to be a brief summary of the design space exploration, with a focus on the final results. The full analysis, which spans hundreds of pages of trade studies, can be found in the PDR and CDR. Each of these documents are publicly available at <http://www.projectfifi.com>.

6.1 Materials

Table 6.1: Material properties for 4 in. diameter tubes

Type	Strength (KSI)	Density (lb/in^3)	Cost (\$/in)
Cardboard	N/A	0.044	0.70
Blue Tube	N/A	0.037	0.81
Fiberglass	30	0.061	1.89
Carbon Fiber	120	0.056	4.90

Of the four materials considered, Carbon Fiber offered the highest strength but was also the highest cost and could cause interference with radio transmissions. Based on strength, the next choice, would be the fiberglass. This came in two variations that were well suited to rocket construction. Several manufacturers offered G-12 filament wound tubing designed for airframes. These tubes had an extremely high linear strength due to the many layers of wind angles from 30° to 45°. For other components of the launch vehicle, G-10 laminate sheets were available. These sheets had similar mechanical properties to the airframe tubes but

were not filament wound and therefore had unidirectional strength. Blue Tube, which was reinforced cardboard, and traditional cardboard tubes offered mediocre strength but had the best density and cost values.

All four materials were capable of withstanding the longitudinal forces that will act on the rocket during launch, however, cardboard lost the longitudinal strength when the tube was deformed. This deformation can happen at any time during transport or construction, which could cause failure of the vehicle on launch. Fiberglass, Carbon Fiber and Blue Tube were resistant to this kind of damage. Another factor to consider was that both Blue Tube and Cardboard lose structural integrity when they become wet, while the resin composites, fiberglass and carbon fiber, were water resistant.

Tearing resistance was another thing to consider for the materials. When the parachutes are deployed, the sections of the rocket separate with high force and pull the shock cord taught. If the sections of the rocket are not perfectly aligned with each other when the shock cord gets pulled taught, it is possible for the cord to impact the sides of the airframe and cause a tear in the airframe. This is known as the zipper effect and is very common in high-power rockets made from cardboard. Fiberglass and carbon fiber would not tear under these conditions. There is a possibility that one of the composites would shatter, instead of tear, but the likelihood of that happening is considerably lower than that of the cardboard or Blue Tube airframe tearing.

Even though fiberglass was the second most expensive and heaviest of the four materials, the high strength, resistance to deformation and water resistance made it the ideal material.

Table 6.2: Epoxy properties

Type	Cure Time (hrs)	Pot-Life (min)	Viscosity (cps)	Mix Ratio	Min Temp (°F)	Strength (PSI)	Cost (\$/pint)
Tap Marine Grade Epoxy							
Slow	6-6.5	25-30	450	2:1	40	7000	28.95
Medium	5-5.5	20-30	500-700	4:1	75-80	6000	30.45
Fast	2.5-3	12-15	550	4:1	40	9000	31.45
System Three Resin							
1	2	15	1100	2:1	35	7500	24.00
2	4	30	900	2:1	55	7500	24.00
3	9	70	350	2:1	75	7500	23.46

Of the different epoxies compared, most of them had similar mechanical properties. The most important property considered was the strength, since the rocket will experience very high forces. The Tap Marine Grade Epoxy with a fast hardener showed the highest tensile strength but all choices far exceeded what was needed. Second to strength, viscosity was of important consideration. The surfaces that needed bonding were made from fiberglass, which does not bond well chemically. A low viscosity allows epoxy to saturate the roughed fiberglass surface and form an additional mechanical bond, which was especially important in the high stress areas of the rocket. For these reasons, the Tap Marine Slow cure and System Three Resin number 3 were the best epoxies.

The decision to use Tap Marine Grade Epoxy over System Three Resin came down to availability, since both epoxy systems offered similar mechanical properties. The System Three Resin was superior in viscosity and cost, whereas the Tap Marine Grade had more strength and was locally available. The local TAP Plastics store stocked the Marine Grade Epoxy and a selection of additives to vary the mechanical properties, such as milled glass and silica fiber. For these reasons, Tap Marine Grade Epoxy slow cure was the epoxy of choice.

6.2 Airframe

6.2.1 Body

An important aspect of the rocket to consider was how much room is available for the scientific payload. The motor, electronics bay, parachute and nose cone accounted for most of the volume of the rocket. The remaining space was where the scientific payload would reside. A trade study was conducted to determine the optimal mass, length and body diameter that provided sufficient room for a payload bay, indicated by the red section below.

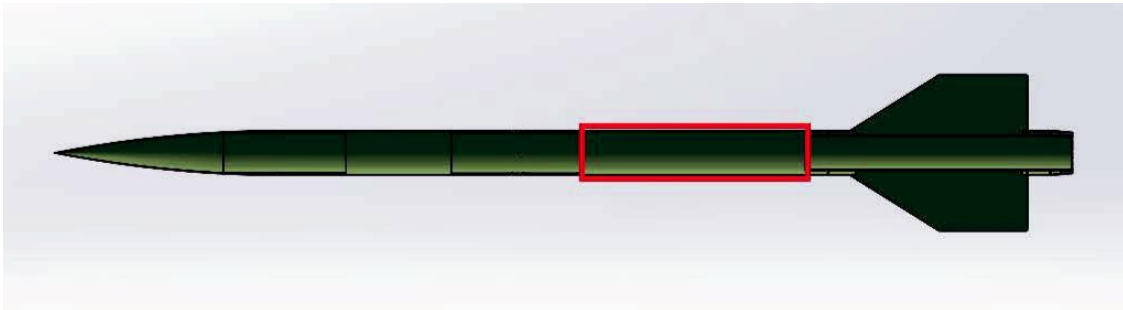


Figure 6.1: Payload section identification

Table 6.3: Weight of G-12 at various lengths and diameters

Weight	4 in	5.5 in	8 in	Volume	4 in	5.5 in	8 in
90 in	12.43	17.91	23.51	90 in	157.07	257.21	296.06
95 in	13.15	19.04	24.97	95 in	192.29	316.70	336.20
100 in	13.51	19.60	25.69	100 in	227.52	376.18	576.35

Units are lbf and in^3 respectively

Based on the impulse limitation of $5,120 \text{ N} \cdot \text{s}$, all 8 in. diameter choices were ruled out. The return on length per weight was greater than diameter so length was favored over diameter. When construction was considered, the 5.5 in. diameter was ideal to work with but at 100 in., the weight gain was unacceptable given the available thrust. For the purpose of reaching the 1 mile altitude target, the 100 in. length and 4 in. diameter options were chosen.

6.2.2 Nose

For nose cones, there were three main options commercially available: conical, tangent ogive, and Von Karman ogive. As seen in Figure 6.2, the Von Karman provided the lowest drag in the transonic region for the ones available. As far as internal volume, the Von Karman and conical both had lower internal volumes than the tangent ogive. Due to the of the electronics stored in the nose cone, the tangent ogive was a better choice because of the larger internal volume. Based on the formulas that define an ogive, maximum internal volume was calculated from slenderness (2^L_R). By integration in terms of y , a slenderness ratio of 5:1 was determined to be optimal.

$$\rho = \frac{R^2 + L^2}{2R} \quad (6.1)$$

$$y = \sqrt{\rho^2 - (L - x)^2} + R - \rho \quad (6.2)$$

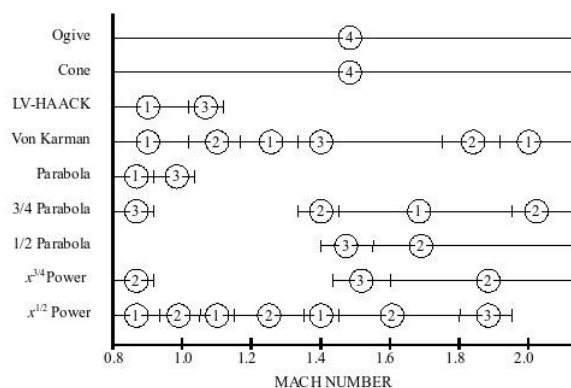


Figure 6.2: Comparison of drag characteristics of various nose cone shapes in the transonic to low-mach regions. Rankings are: superior (1), good (2), fair (3), inferior (4). [7]

6.2.3 Stability

Previous to the development of spin stabilization and thrust vectoring, rockets used fins for stability. There were two primary purposes to fins, shift the center of pressure aft and provide a restoring moment when the rocket experienced an angle of attack. For a rocket to be considered stable, the center of pressure needed to be located at least two body diameters aft of the center of gravity. The Barrowman equations were used to calculate a distance from the tip of the rocket to the center of pressure for two fin designs.

L_N = length of nose
 d = diameter at base of nose
 d_F = diameter at front of transition
 d_R = diameter at rear of transition
 L_T = length of transition
 X_P = distance from tip of nose to front of transition
 C_R = fin root chord
 C_T = fin tip chord
 S = fin semispan
 L_F = length of fin mid-chord line
 R = radius of body at aft end
 X_R = distance from fin root leading edge and fin tip leading edge parallel to body
 X_B = distance from nose tip to fin root chord leading edge
 N = number of fins

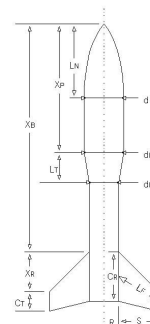


Figure 6.3: Barrowman

$$(C_N)_N = 2 \quad (6.3)$$

$$\text{Cone} : X_N = 0.666L_N \quad (6.4)$$

$$\text{Ogive} : X_N = 0.466L_N \quad (6.5)$$

$$(C_N)_T = 2 \left(\frac{d_R}{d} \right)^2 - \left(\frac{d_F}{d} \right)^2 \quad (6.6)$$

$$X_T = X_P + \frac{L_T}{3} \left[1 + \frac{1 - \frac{d_F}{d_R}}{1 - \left(\frac{d_F}{d} \right)^2} \right] \quad (6.7)$$

$$(C_N)_F = 1 + \frac{R}{S+R} \frac{4N \left(\frac{S}{d} \right)^2}{2L_F} \quad (6.8)$$

$$X_F = X_B + 3^R \frac{(C_R + C_T)}{X(C_R + 2C_T)} \frac{1}{6} \frac{(C_R + C_T)}{C_R} + \frac{C_T}{C_R} \quad (6.9)$$

$$X = \frac{(C_N)_N X_N + (C_N)_T X_T + (C_N)_F X_F}{(C_N)_N + (C_N)_T + (C_N)_F} \quad (6.10)$$

Based on the Barrowman equation set, the center of pressure (denoted by the red circle) of each fin design is compared against the center of gravity (denoted by the blue and white circle).

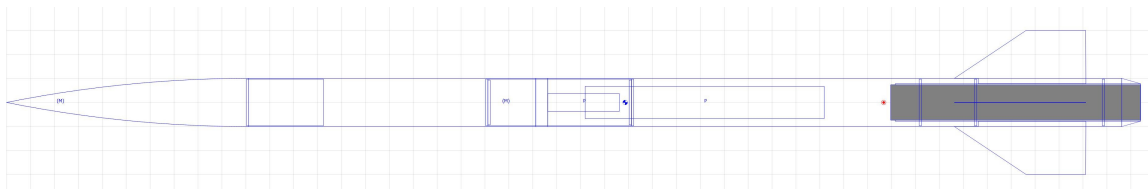


Figure 6.4: Old fin stability diagram

The original fin design shown in Figure 6.4 had a C_p 73.34 in from the nose and a C_g of 51.72, resulting in a 5.37 stability factor. Although this is quite stable, the rocket was designed to accommodate many different scientific payloads which may vary in weight so the fins were redesigned to improve the stability.

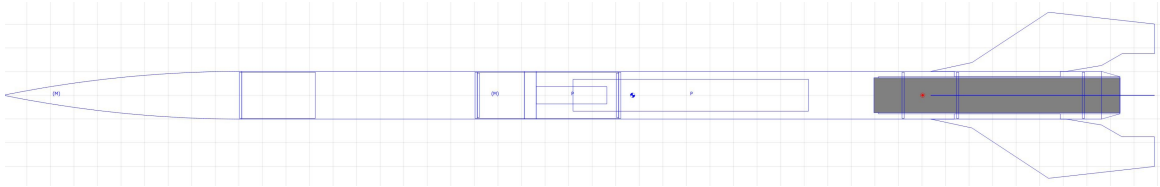


Figure 6.5: New fin stability diagram

The new fin design, shown in Figure 6.5, gave the rocket a platform to stand on vertically and shifted the C_p further aft, which improved stability. With the more surface area towards the rear of the rocket, the C_p moved to 78.06 in from the nose and provided an superior stability factor of 6.12.

6.2.4 Summary

The airframe of the rocket was constructed of commercially available G-12 fiberglass tubes, while other components, such as the bulkheads, caps, centering rings, and fins, were CNC machined from G-10 fiberglass laminate. All fixed components were bonded with a TAP Marine Grade epoxy mixture appropriate for the application. Depending on application, various additives were also added to the epoxy mixture. For all structural joints, milled glass fiber was used to strengthen the matrix. Fine silica fiber was also used to vary the thixotropic property depending on the area of application.

Dimensionally the airframe had a consistent major diameter of 4 in. until the tail cone taper, which diminished to just over 3 in. The upper and lower airframe sections were 24 in. and 48 in. respectively. The payload, motor mount tube, and half of the electronics bay resided in the lower airframe. The motor mount tube was a 21 in. long, 3 in. (75 mm) diameter tube located in the aft section of the lower airframe. Due to the high amount of initial thrust, three centering rings joined the

motor mount tube to the airframe. Two of the centering rings were strictly for structural integrity, while the third also acted as a keyed mounting system for the payload. The payload bay was a 21 in. section located between the motor mount tube and electronics bay. The upper airframe contained a 15 in. long section for the recovery system. Since the rocket was not designed to go supersonic, an ogive nosecone of 5:1 ratio was selected to accommodate the additional electronics housed in the nose cone. The nose cone was filament wound G-12 fiberglass with an aluminum tip. The inside of the tip was also threaded for a steel rod that ran the inside length of the nosecone, which secured the closure and electronics sled. The modified four-fin design was inspired by modern stealth aircraft and featured a sleek angular design. The fins were shifted aft of the rocket to move the center of pressure further back to compensate for the payload also shifting the center of gravity back. The fins had an overall length of about 17 in. by 5.5 in., which produces a stability margin above 6. Since the trailing edge of the fins had little affect on rocket performance, the back section of the fins were flattened to allow the rocket to rest upright. The completed airframe has a dry weight of 17 pounds, which impacts the motor selection.

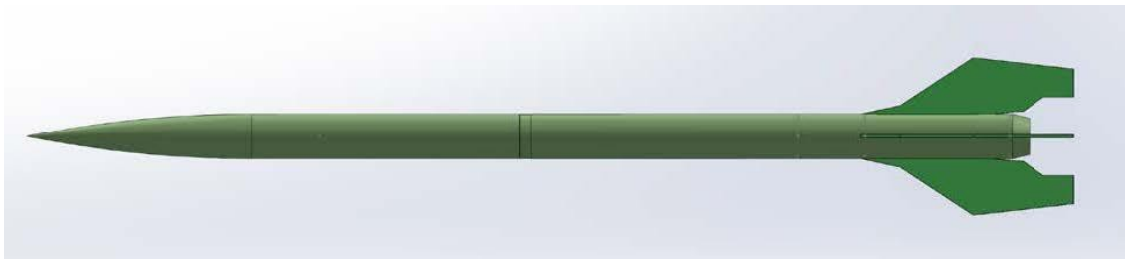


Figure 6.6: Final airframe design

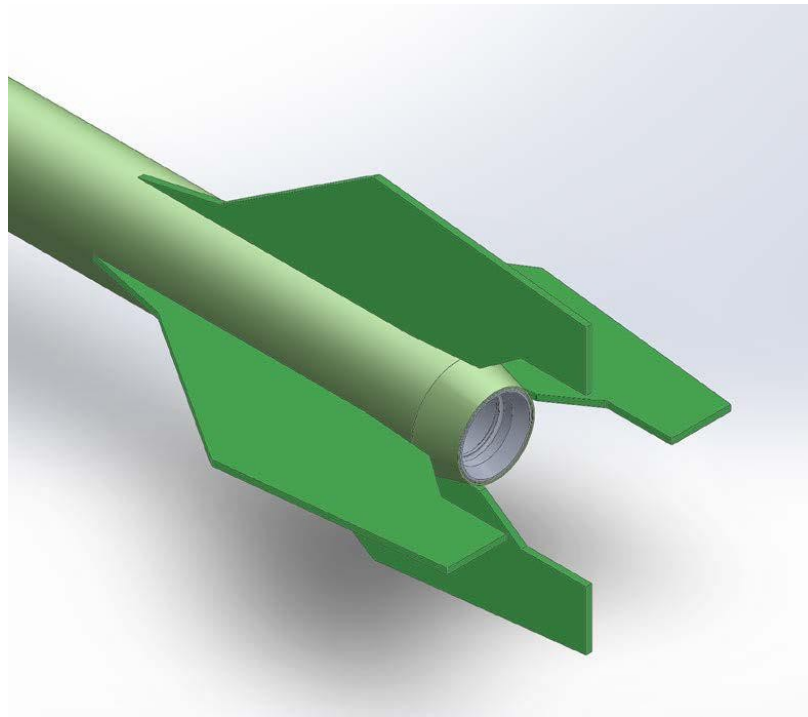


Figure 6.7: Final fin design

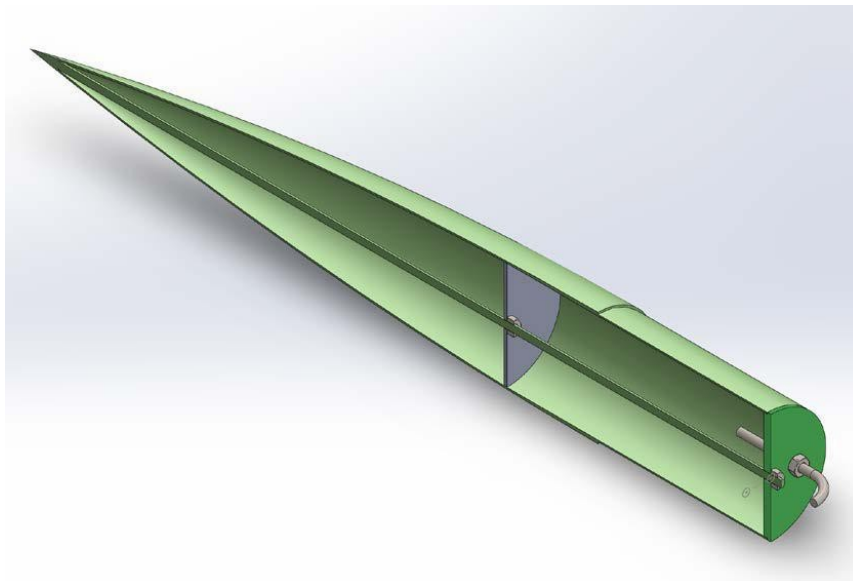


Figure 6.8: Cut-away of nose

6.3 Propulsion

In order to determine the optimal propulsion system for the launch vehicle, the respective design space was explored. If the rocket was still being used for competition, motor selection would have been limited to solid. Since the purpose was modified to a scientific research vehicle, other propulsion types were considered. Parameters of the space consisted of propellant type, re-usability, impulse class, maximum velocity, rail-exit velocity, thrust to weight ratio, maximum altitude, and manufacturer.

There are three primary propellant types available; solid, liquid, and hybrid. Solid has the advantage of being readily available and is the least complex to construct. The simplicity of solid is largely related to how the oxidizer and fuel are already combined in the propellant grains. While this makes the setup and construction of the motor easier, it also prohibits the motor from being stopped once ignited and introduces additional hazards of being highly explosive. Liquid rocket engines use separate oxidizer and propellant, which is mixed in the combustion chamber. These engines have the advantage of being able to be stopped and restarted but require extensive additional hardware. As expected, hybrid motors are a combination of solid and liquid. The solid fuel is lacking built-in oxidizer and thereby not as hazardous and fairly inert while not in use. A hybrid engine shares the start and stop ability with the liquid engine but requires less additional hardware. Since the primary purpose of this launch vehicle is to fly various science payloads, the use of a solid motor provides more cargo space by lacking the additional propulsion hardware that is needed for liquid or hybrid engines. Additionally, solid propellant is easier to acquire and for these reasons, a solid motor is the propulsion system of choice.

One classification of motors is by life-cycle, namely single-use or reusable. Like most options, there are several pros and cons for each style. Reusable motors have a separation between motor hardware and propellant. The advantage to reusable is that only the consumables are being replaced between launches, which reduces long term cost. Additionally, the hardware can be machined to a higher grade, which does add to the initial cost but also decreases the chance of catastrophic failure (CATO). All of these advantages do come at a cost, both in initial price of the hardware and additional construction time needed to assemble the motor prior to launch. The disposable motors are cheaper initially and require less setup. Unfortunately, the disposal of the entire motor means that potentially reusable components are made cheaper and are also being discarded. There is also a slight hazard difference between the motor styles; reusable propellant is stored in separate sealed sections and is less prone to inadvertent explosion as compared to disposable motors, which are fully ready to ignite. It should also be noted that the selection of disposable motors is far more limiting than the reusable style. Based on the long term research use of the rocket, reusable motors are a better choice. The long term savings warrant the higher initial cost.

After choosing to use a reusable motor, the next parameter to explore is impulse class. Rocket motors are classified by total impulse and assigned letter designations. Each subsequent letter corresponds to roughly double the total impulse of the previous. The typical solid rocket motors found in hobby stores range from class A to class F. Motors of class H and higher (160 Ns or greater) are classified as high power and require a license from either National Association of Rocketry (NAR) or Tripoli to use. In each of the organizations, there are three respective levels to which the maximum usable impulse class is dictated. Based on the highest license holder in the group, motor choice is restricted to class L or

below. From the predicted dry weight of the rocket and a target altitude of the mission in excess of 5,280 ft, a class L motor is the optimal choice.

Since there are dozens of class L motors, specific selection is dependent on manufacturer and respective thrust curves. The primary makers of commercially available solid rocket motors are Cesaroni and Aerotech. Due to an explosion of a storage facility, supply of Cesaroni motors are extremely limited and thus Aerotech is the better choice. Evaluation of each Aerotech class L motor is based on experimentally derived thrust curves. When a solid motor burns, there is a pattern associated with the change in thrust. There are three basic burn patterns: progressive, regressive, and neutral. The thrust increases over time in a progressive motor, decreases for a regressive, and stays relatively constant for neutral. Thrust curves are a visual representation of these burn patterns and help to evaluate the appropriate style for a given set of requirements.

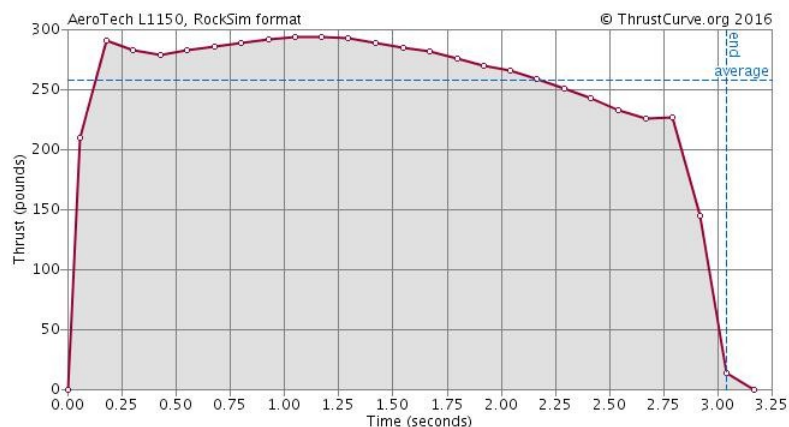


Figure 6.9: Aerotech L1150R thrust curve

For this launch vehicle, there are two primary parameters that need thrust curve investigation. For the rocket to have a stable liftoff, the motor needs to provide enough initial thrust to weight to ensure that the launch vehicle exits the

guide rails with sufficient velocity for fins to provide a restoring moment and correct perturbations. As a general rule, a minimum of 52 ft/sec upon rail exit is considered sufficient. Since this vehicle is being launched from 12 ft. 1515 rails, an initial thrust to weight of 8:1 is required. In addition to providing sufficient thrust to weight for stable launch, the motor must not accelerate the vehicle to supersonic speeds because the scientific payload is designed for subsonic research. Final motor selection is based on flight simulations conducted by taking the launch vehicle model and performing numerical integration with each potential thrust curve.

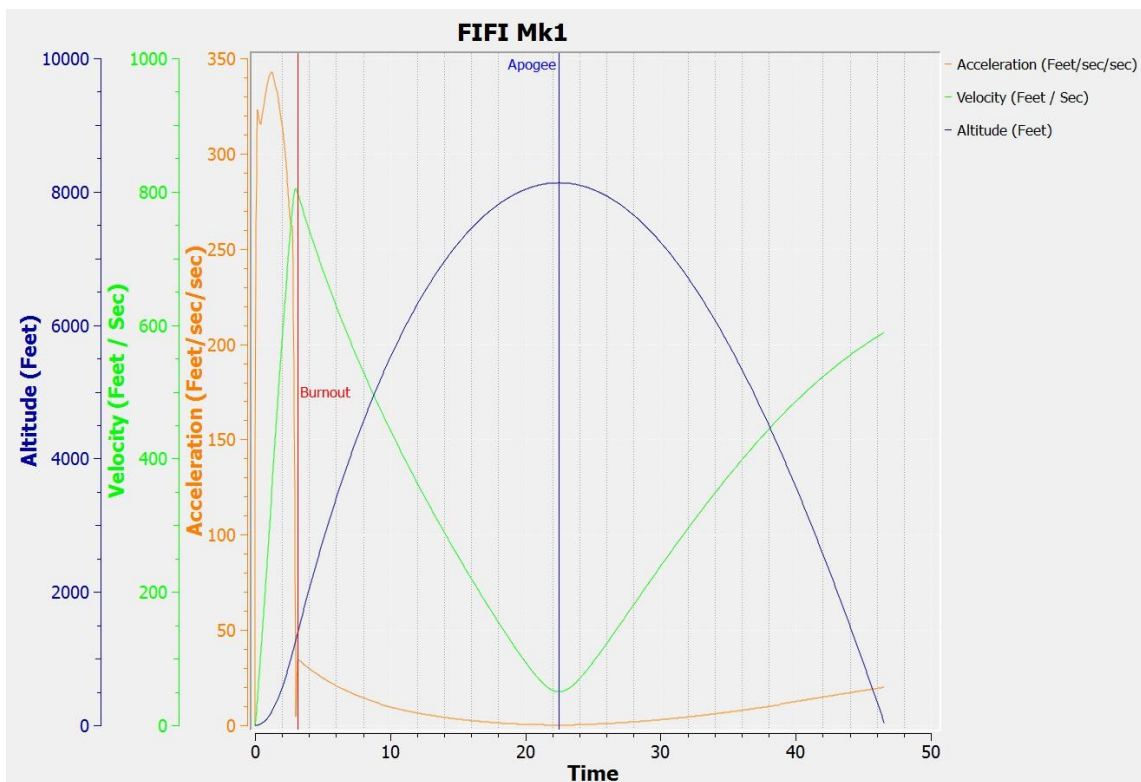


Figure 6.10: Flight simulation plot

Based on resulting flight data from the simulations, an Aerotech L1150R provides sufficient initial thrust to exit the rail at over 70 ft/sec, while also staying subsonic all the way to apogee at roughly 8,000 ft.

6.4 Recovery

The rocket was designed to have multiple recovery configurations possible depending on the payload being flown and launch day conditions. If drift was a concern, such as during windy conditions, dual deployment could be utilized. In this scenario, a small drogue parachute would be deployed at apogee to allow for a controlled high-speed descent. At a predetermined altitude, generally about 600 ft., the main parachute would be deployed and the vehicle would slow to a safe landing speed. The alternate scenario, single deployment, forgoes the drogue and simply deploys the main at apogee. For this flexibility, the airframe was designed to have two separation points, just below the nose cone and below the electronics bay.

Due to the fragile nature of the sensor payload being flown on the maiden flight, single deployment was chosen to avoid parachutes and separation near the upper airframe strain gauges. The upper section was secured to prevent separation and the parachutes were placed in the lower airframe.

6.4.1 Electronics Bay

The E-Bay consisted of a double sided set of laser cut acrylic sleds where all the electronics were mounted. One side of the sled contained the flight computers, associated batteries and rotary switches used to arm and disarm the system. The other side contained all the circuitry needed to log sensor data during the flight.

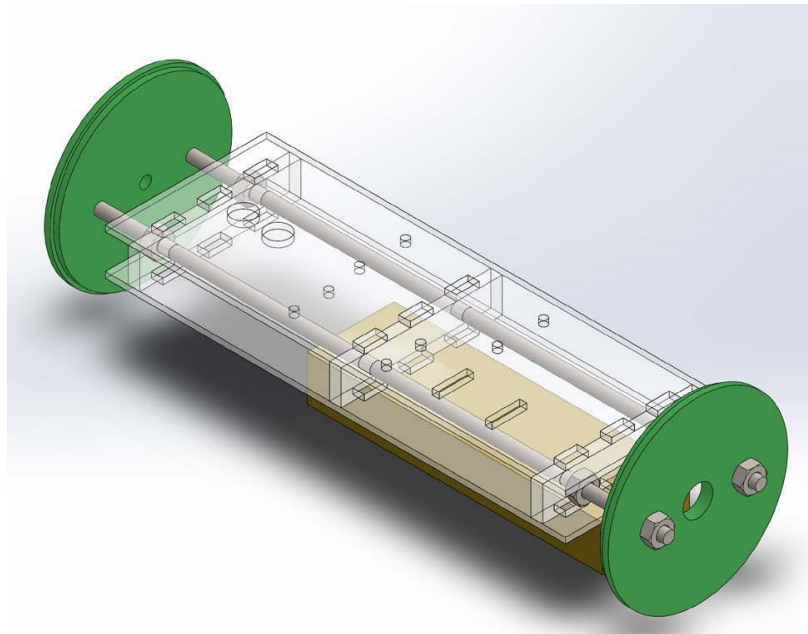


Figure 6.11: Electronics bay

Controlling the separations and ejection charges were two flight computers. The TeleMega acted as the main flight computer, while the Stratologger took the secondary role. The use of two flight computers was for redundancy based on the previous rocket failure discussion. The TeleMega was also used to report back live telemetry data via an amateur radio link. The Stratologger recorded flight data to the on-board storage which was retrieved after the flight.

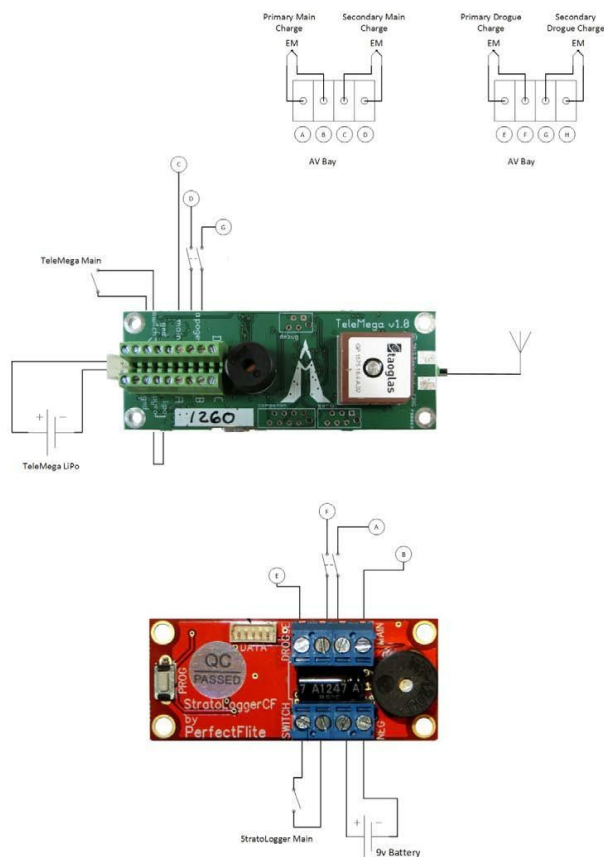


Figure 6.12: Flight computer wiring

6.4.2 Parachute

The mission requirements outlined that all parts of the rocket are required to impact the surface with a maximum kinetic energy of 150 ft-lbf upon landing. Based on an estimated burnout weight of 24 lbs., this resulted in a descent rate just under 20 ft/s. Bounded by this impact energy, parachutes were evaluated based on C_d , shape, packing volume, and cost. The main chosen was a 72 in. Fruity Chutes Iris Ultra because of the toroidal design that offered an impressive C_d of 2.2 and very low packing volume when combined with spectra lines.

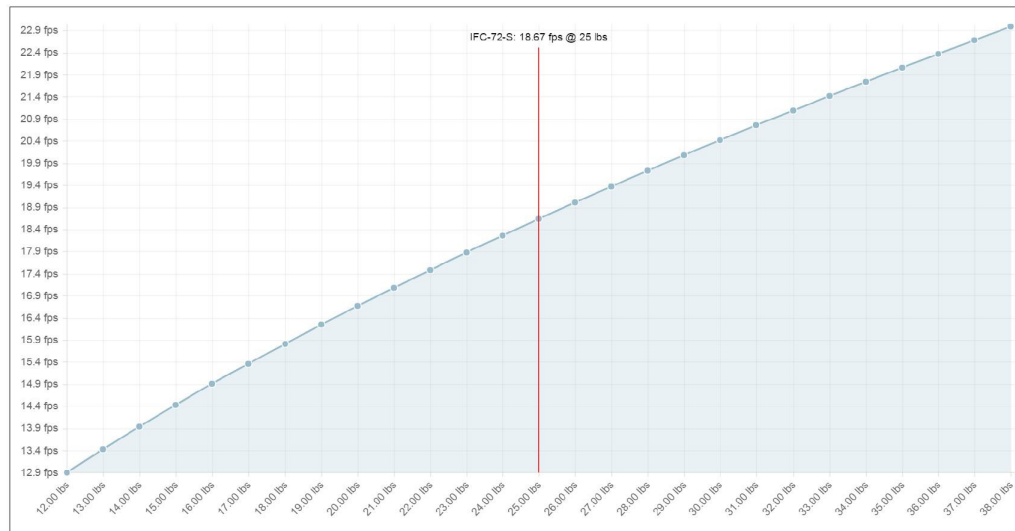


Figure 6.13: 72” Iris Ultra descent vs weight

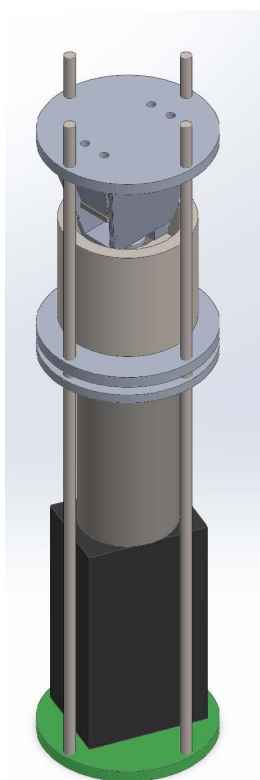
6.5 Payload

The purpose of the launch vehicle was to fly various scientific payloads and thus two different payloads were designed and flown. First, a reaction wheel system was developed to control the longitudinal attitude of the vehicle. Second, the upper airframe was modified to include a sensor array for the measurement of skin friction during subsonic flight.

6.5.1 Reaction Wheel

A reaction wheel is an angular momentum device that controls spin about an axis by the conservation law of angular momentum. The wheel is a disc of high angular inertia, which is spun to an extremely high rpm resulting in enormous angular momentum. Changes to the rpm result in applied torques.

wheel assembly



The initial open-loop system designed consisted of a precision machined stainless steel disc, brush-less electric motor, Castle Creations ESC, Adafruit 10 DOF IMU, Arduino micro-controller, and SD card/reader for data logging. Schematics of these items are included in Appendix B. Prior to launch, the ground station sent an initialization signal via amateur radio, that caused the wheel to spin up to 16,000 rpm. This gave the system a high starting angular momentum and also added to the rocket stability.

The next stage of the sequence was post burnout, which was determined by the IMU. Once detected, the micro-controller sent a signal to the ESC to reduce the motor rpm. Conservation of momentum caused a reverse torque to be

Figure 6.14: Reaction generated when the motor tried to slow the wheel. Transfer of torque between the reaction wheel system and rocket airframe was accomplished by the keyed housing system shown in Figure 6.14. Due to size constraints, the reaction wheel system shared space with the electronics bay as seen in Figure 6.15

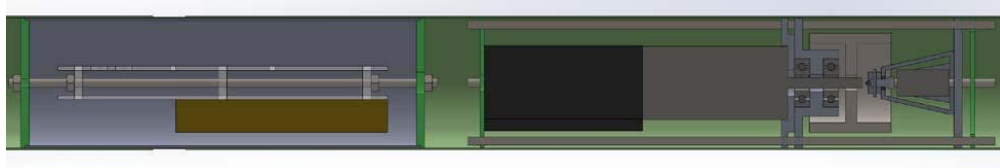


Figure 6.15: Reaction system placement

The open loop reaction wheel system operated on predetermined rpm values and thus could not fully control the longitudinal axis as intended. Although development was not completed due to the payload change, a closed loop control system was started. The basic controller setup shown in Figure 6.16, was for the micro-controller to process IMU data and vary the ESC to the desired angular rate.

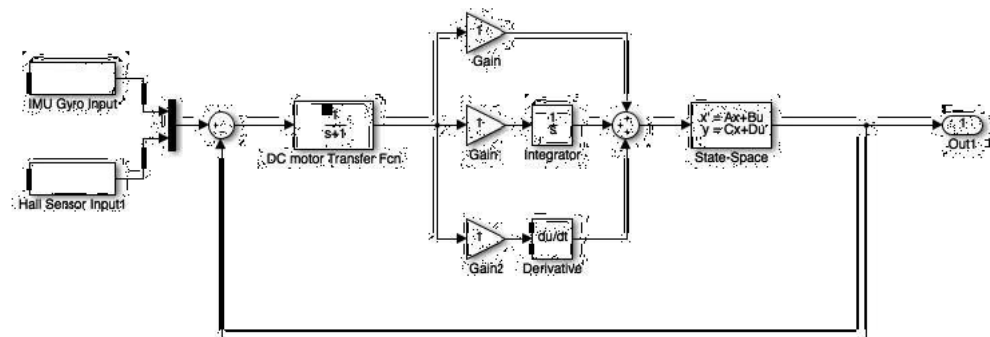


Figure 6.16: Simulink controller design

6.5.2 Sensor Package

Several sensor options were considered to collect aerodynamic data during subsonic flights. The first proposed option was a pressure sensor design that consisted of 3 sets of pitot tubes arranged as a rake normal to the outside airframe. Pressure measurements taken at different distances from the surface would help to study the boundary layer. Due to limitations getting small enough pitot tubes, the pressure sensor design was abandoned in favor of a strain gauge setup. Instead of reading the pressure variation within the boundary layer, the sensor package would read skin friction at the surface.

Multiple sets of strain gauges were equidistantly fixed around the upper

airframe to form a sensor ring. Each set consisted of a matched pair of strain gauges, referred to as active and passive. The active strain gauge was aligned parallel to the free-stream, while the passive was set perpendicular. By having the gauges set 90° apart, strain caused by temperature was eliminated from the results. For each pair of active and passive strain gauges, there was a matched reference set on the inside of the rocket. All of the sensor sets were wired to an Arduino with an SD card/reader to record data.

A strain gauge acts as a variable resistor that changes resistance based on deformation. The specific strain gauges used here were the OMEGA SGD-5/350-LY11 Precision Strain Gauges. Each LY-11 gauge had a nominal resistance of $R = 350\Omega$. Resistance varied linearly with axial strain, according to the following Gauge Factor (GF) relationship:

$$GF = \frac{\Delta R}{R} \quad (6.11)$$

Gauge Factor is a constant based on several factors but based on industry standard, approximately $GF = 2$ is recommended. The LY-11 strain gauges used had a $GF = 2.13$, which was within industry standards. The Gauge Factor equation was reorganized into a more useful form since change of resistance was measured by the strain gauges.

$$\Delta R = GF \cdot \epsilon \cdot R \quad (6.12)$$

Based on preliminary calculations, strain was expected to be on the order of $= 10^{-5}$ or smaller. The corresponding change in resistance was expected to be incredibly small and difficult to measure. To compensate for the nearly immeasurable resistance changes, sets of four strain gauges were paired to form Wheatstone bridges. A Wheatstone bridge, shown in Figure 6.17 consists of four resistors and two voltage dividers, that when compared, convert resistance

differences into voltage potential.

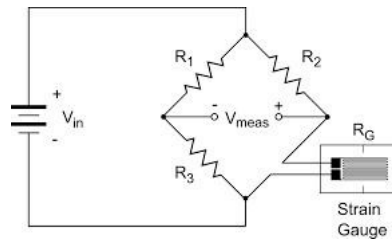


Figure 6.17: Wheatstone bridge circuit

The voltage difference, referred to as V_{meas} , between each of the voltage dividers was found using the following formula:

$$V_{meas} = V_{in} \left(\frac{R_3}{R_1 + R_3} - \frac{R_G}{R_G + R_2} \right) \quad (6.13)$$

Since the resistance change was expected to be similar in magnitude to the strain caused by ambient temperature change, the R of the passive gauges was neglected to compensate. The next issue was converting the analog signal from the sensors, into a digital signal that was usable. An Arduino can take an analog input between 0 and 5 volts, and convert it to a digital value between 0 and 1023, but with only an accuracy of approximately 5mV per unit. The expected voltage difference caused by strain was only between 10-20mV, so additional signal processing was needed. For improved sensitivity, an additional signal processing unit was integrated into the system to boost the voltage difference into the 0 to 5 volt range. The op amp chosen for this was an INA125P instrumentation op amp because of stability and selectable precision voltage reference and gain. The calculated gain needed to boost the signal into readable range was 190. Although this corresponded to approximately 321 Ω , a resistance of 330 Ω was selected for convenience with only a 6 gain loss. The INA125P required a reference voltage of 5V, which was taken from pin 15 of the

Arduino. Additionally, the signal processor needed a stable voltage supply at least 2.5V above the reference, and for this reason, the INA125P was wired to the main power harness that supplied the Arduino voltage as well. A sample rate of 10Hz was selected to stay low in the operating range of the processing units and prevent electronic noise from bleeding into output data. Data from the two bridges was logged to the SD card as port and starboard.

CHAPTER 7

SIMULATION

7.1 Computational Fluid Dynamics (CFD)

Computational Fluid Dynamics (CFD) techniques were used to examine the general aerodynamics of the launch vehicle. Key points of investigation were, stagnation points, high points in fluid velocity, and general flow characteristics. The commercial CFD package, Star-CCM+, was used for all simulations. Grid independence was established by comparing coarse and fine grids before settling on a computational domain of 3.5 million grid points shown in Figure 7.1. Since all flow was subsonic, the control volume, seen in Figure 7.2, was modeled as a bullet.

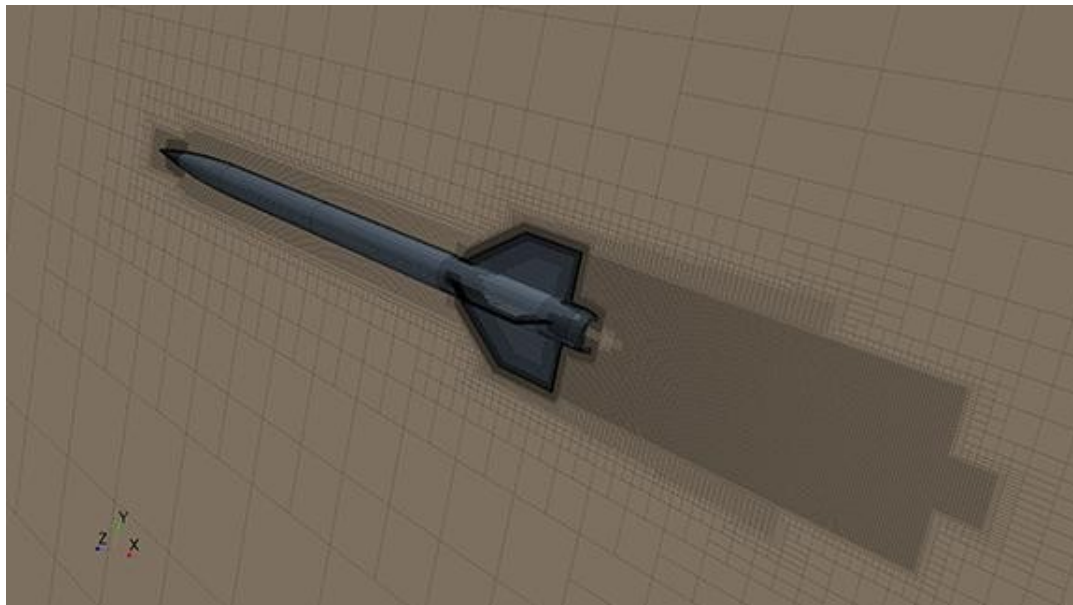


Figure 7.1: Computational mesh

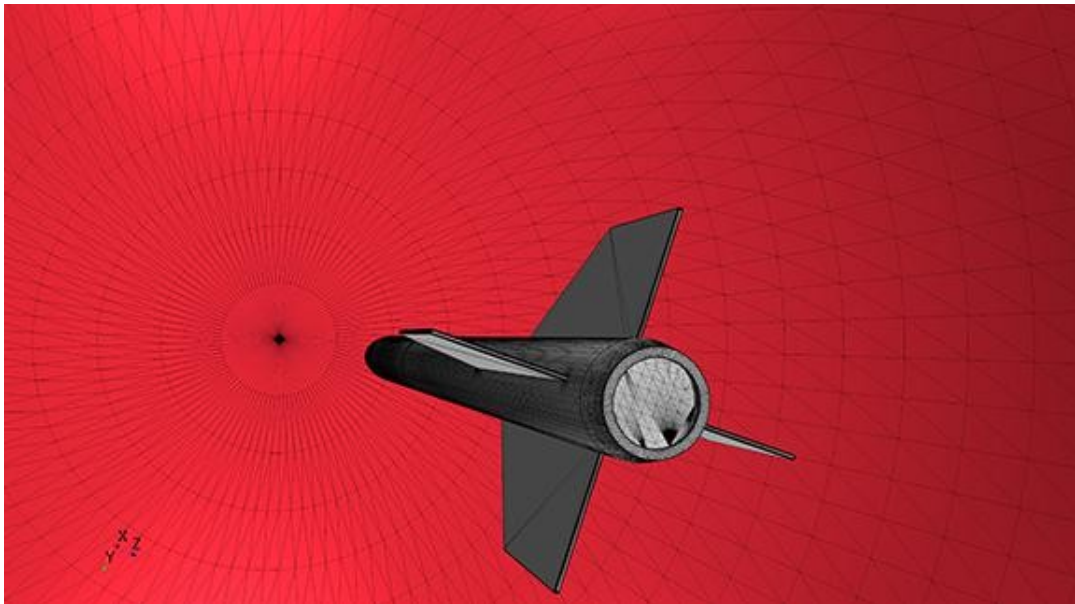


Figure 7.2: Control volume

The converged solution showed exactly what was already expected. The velocity profile, shown in Figure 7.3, demonstrated that the stagnation region aft of the lower airframe was reduced due to the tail cone. Due to the overall slenderness of the body and nose cone shape, Figure 7.4 showed very few high pressure regions.

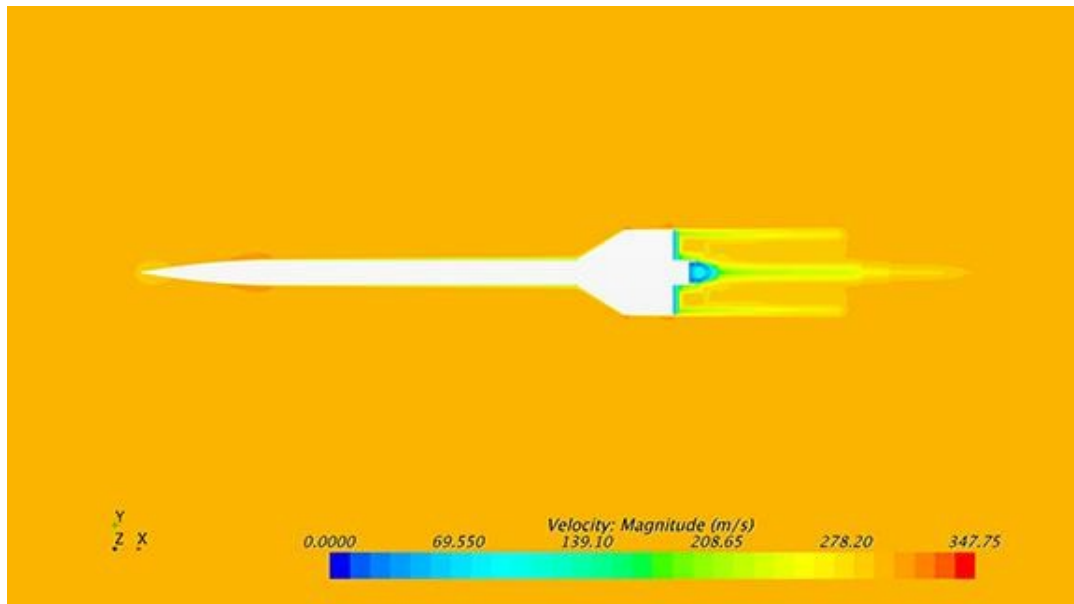


Figure 7.3: Velocity profile

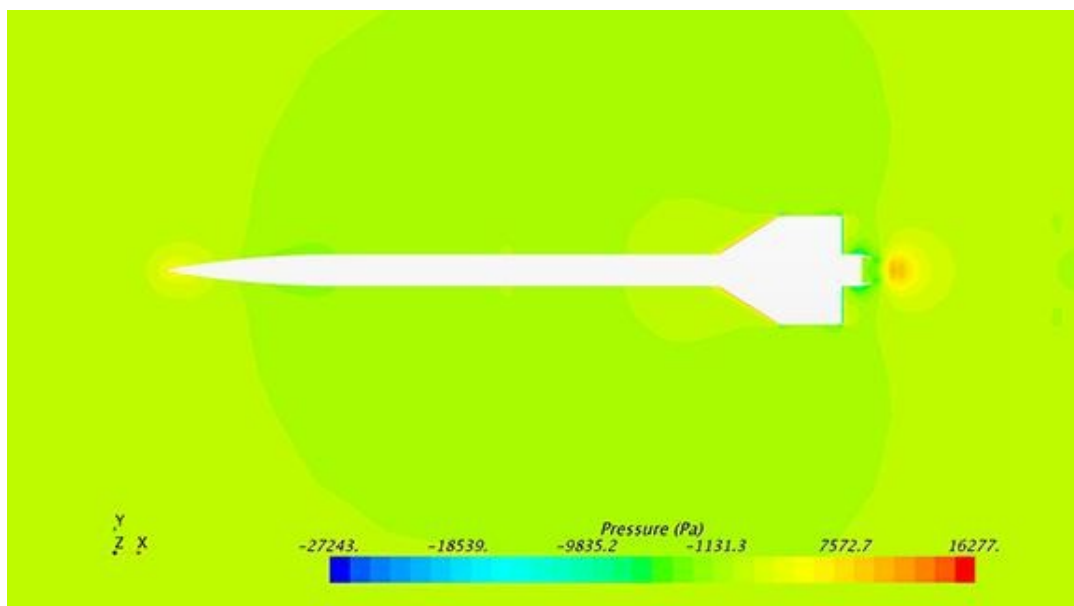


Figure 7.4: Pressure profile

7.2 Finite Element Analysis (FEA)

Finite Element Analysis was used to determine the stress placed on the airframe when subjected to propulsive forces. All simulations were conducted in Solid Works 2016. A force greater than peak motor thrust was applied to a quarter section of the symmetric airframe. Based on the results shown in Figure 7.5 and Figure 7.6, the airframe showed virtually no stress.

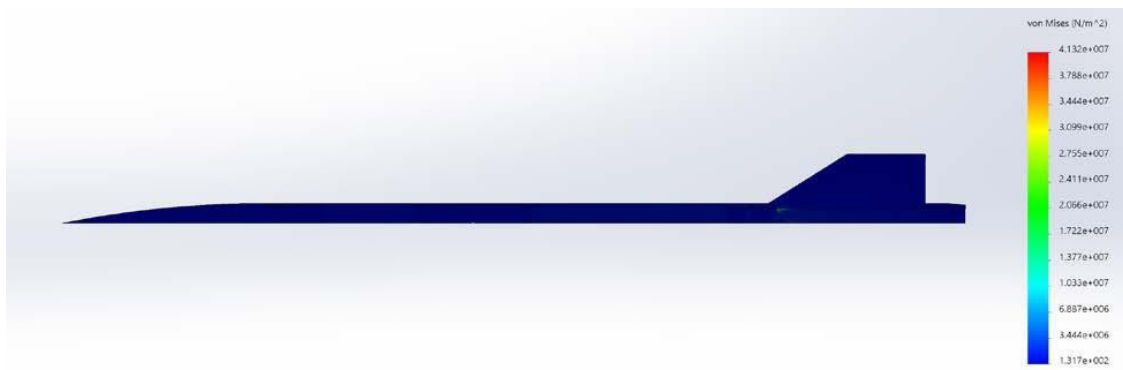


Figure 7.5: Structural analysis of airframe

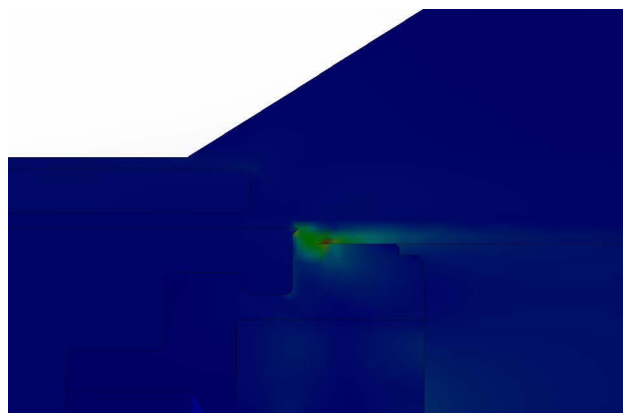


Figure 7.6: Close-up of stress region

CHAPTER 8

RESULTS

8.1 Sub-scale Flight

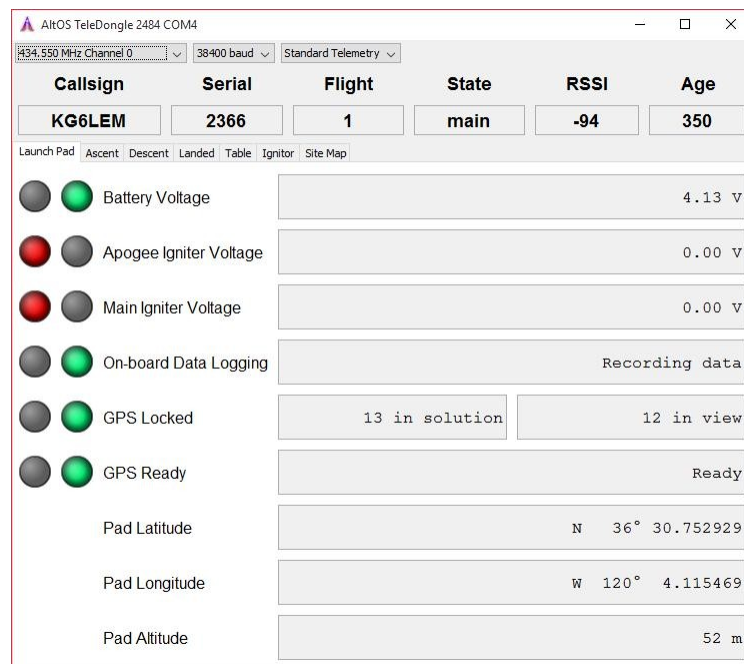


Figure 8.1: Sub-scale telemetry - launch pad

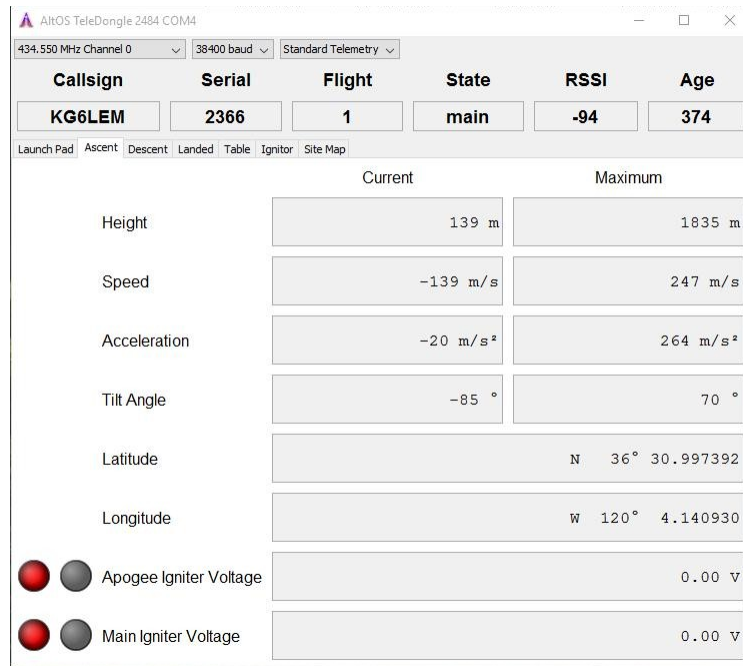


Figure 8.2: Sub-scale telemetry - ascent

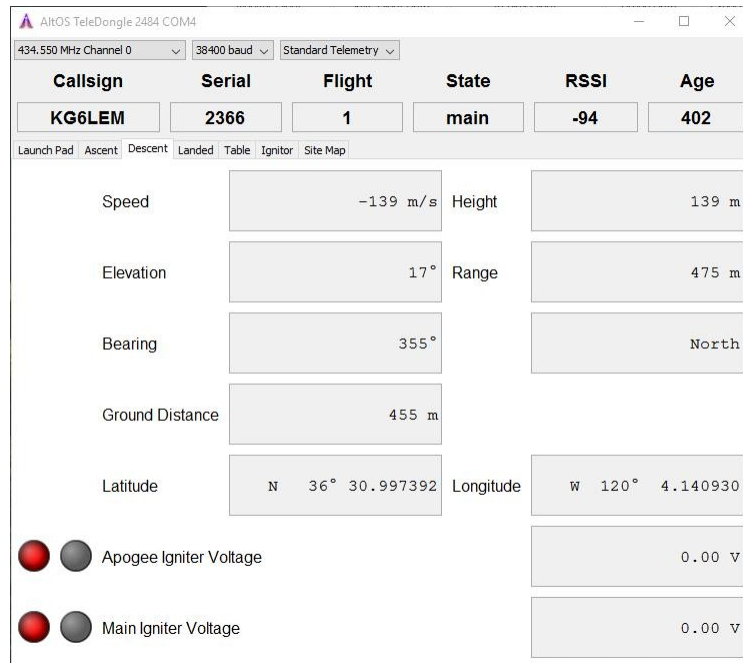


Figure 8.3: Sub-scale telemetry - descent

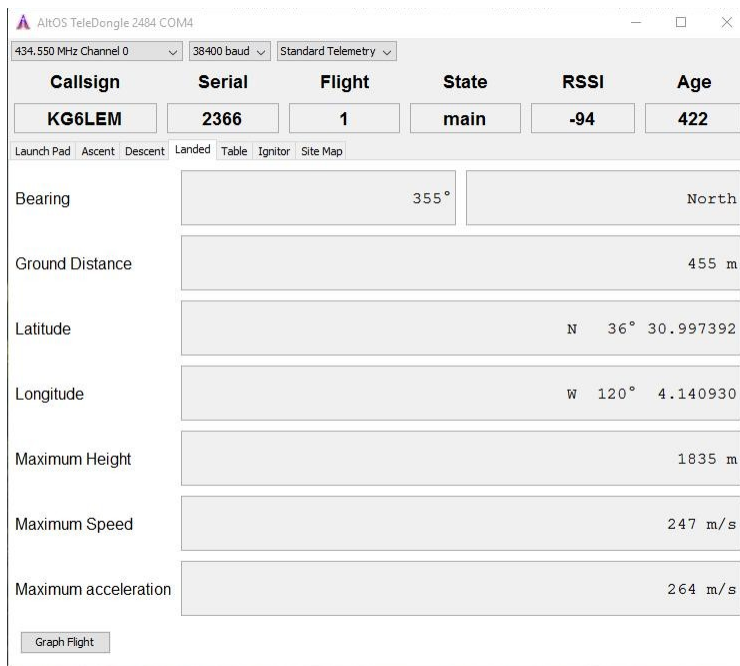


Figure 8.4: Sub-scale telemetry - landing

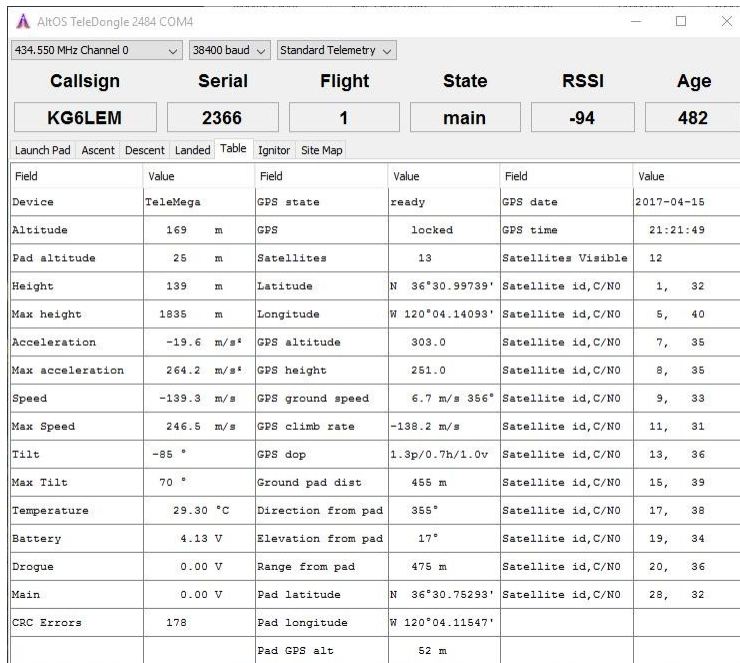


Figure 8.5: Sub-scale telemetry - summary

8.2 Fullscale Flight

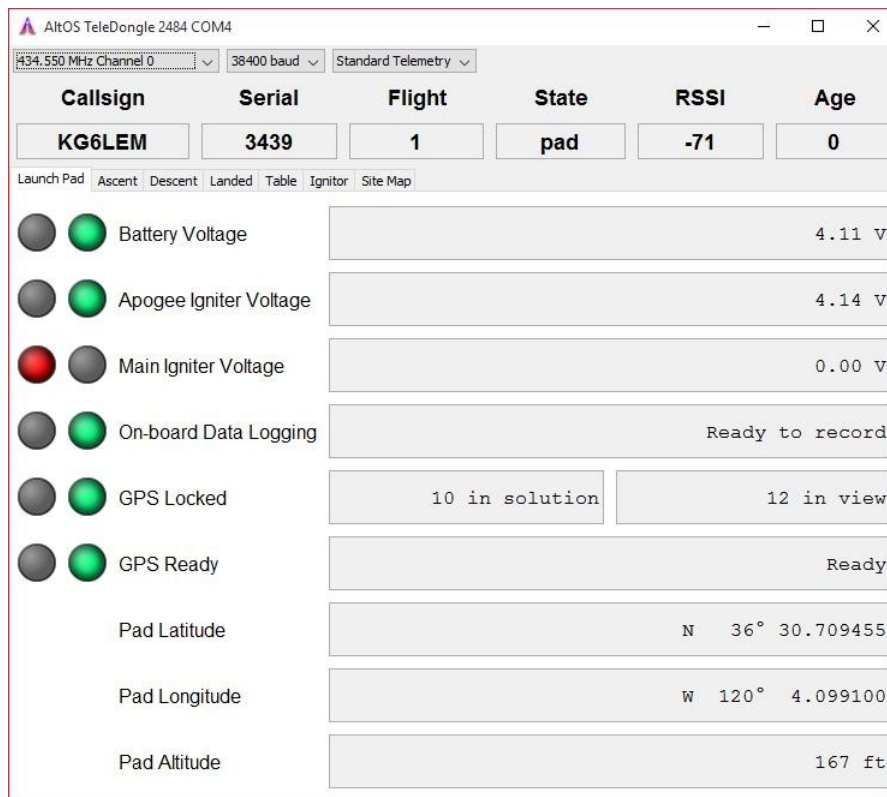


Figure 8.6: Full-scale telemetry - launch pad

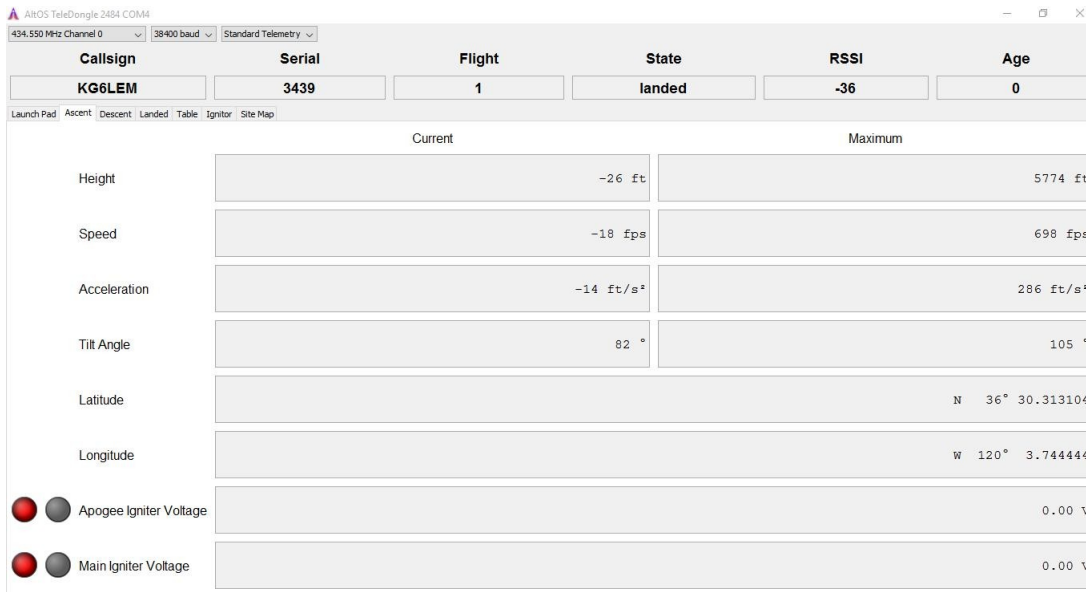


Figure 8.7: Full-scale telemetry - ascent

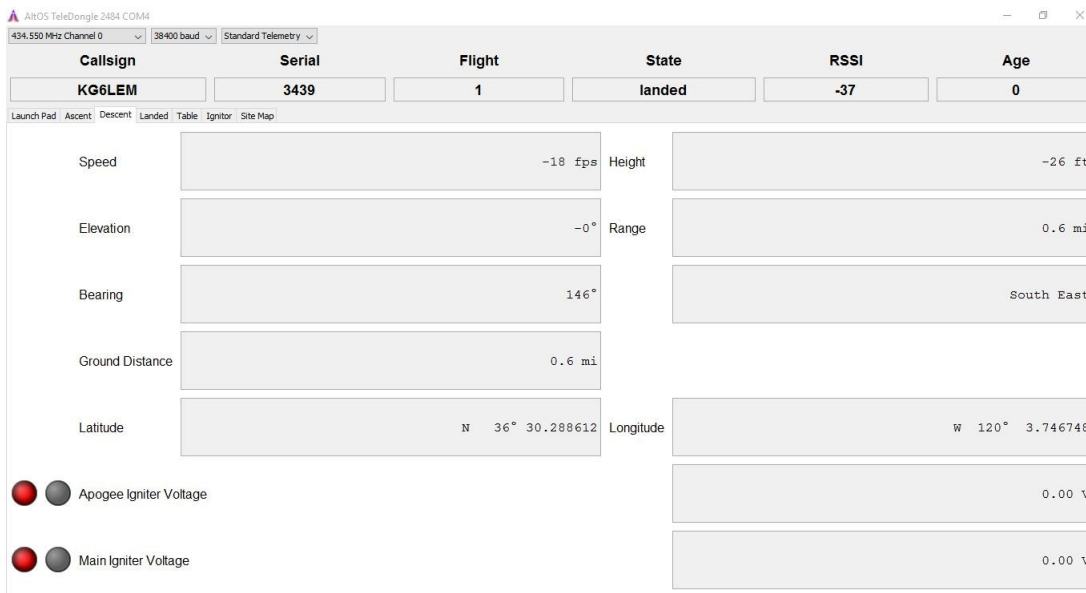


Figure 8.8: Full-scale telemetry - descent



Figure 8.9: Full-scale telemetry - landing

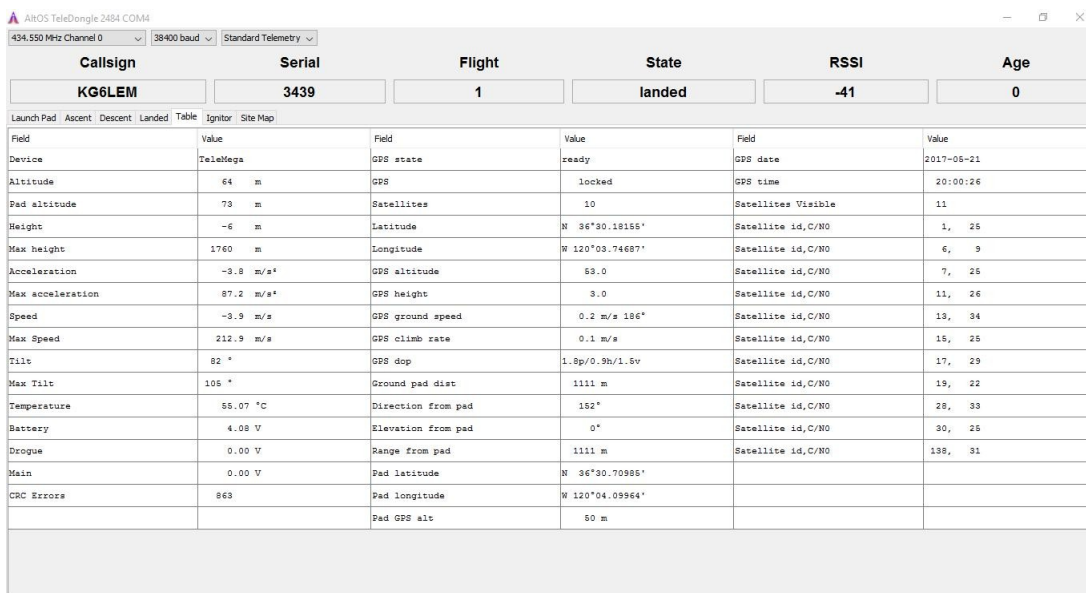


Figure 8.10: Full-scale telemetry - summary

CHAPTER 9

DISCUSSION

Prior to the construction of the full-scale, a sub-scale prototype was built and flown in Helm, CA. All parameters of the rocket were scaled by the ratio 2.6:4, based on body diameter. The only parameter not scaled was the target altitude. Based on flight simulation, the target altitude would be reached with a calculated $825 N \cdot s$ total impulse. The closest total impulse match in the 38 mm category, was an Aerotech J575FJ motor. At just over $800 N \cdot s$ total impulse, the predicted apogee was 5,063 ft. Unfortunately, that motor was not available and the closest substitute was an Aerotech J825R. At $928 N \cdot s$, the predicted altitude was 6,068 ft. High-speed footage of the launch showed a perfect motor ignition followed by a stable rail exit. Confirmed by telemetry, the true apogee of 6,020 ft., shown in Figure 8.2 was less than 1% from the predicted altitude. Although ascent was near perfect, descent was quite the opposite. As noted before, the primary cause of amateur rocket failure, was recovery malfunction. In this case, even redundant flight computers did not prevent the crash and destruction of the rocket. This was a case where telemetry data proved to be invaluable, since all data logging circuitry was destroyed upon landing. The descent telemetry shown in Figure 8.3 confirmed that parachutes did not deploy at apogee, which resulted in a ballistic 139 m/s landing. Research into the voltage history of each blasting charge, revealed open circuit voltage moments after launch. This is consistent with either the charge detonating, or wiring disconnecting. Since a premature detonation was witnessed as high speed separation, the latter must have been the cause. Though not confirmed, it was

suspected that the use of solid core wiring allowed the blasting charge connection to be severed when subjected to the high g-force of launch. As part of the sub-scale launch, a prototype of the open loop reaction wheel payload was flown. Since roll induction was to be initiated by an additional pyrotechnic charge and no rolls were observed, it was assumed that the payload suffered the same wiring failure as recovery.

Based on lessons learned from the prototype launch, the recovery system wiring was redesigned. The solid core wiring was replaced with stranded and all connections were soldered to prevent slipping when subjected to high acceleration. Additionally, since the payload was exchanged for the sensor package, the payload and recovery sections needed to exchange places. This was to prevent any recovery hardware from damaging the delicate sensors. Due to the weight difference between the sensor package and recovery equipment, the rocket balance needed to be reevaluated. A ballast weight was added inside the tip of the nose cone, to shift the C_g forward and increase static stability. A couple months following the sub-scale prototype launch, the full-scale launch vehicle was also flown in Helm, CA. Launch performance was nominal, though ascent exhibited a slight tilt. Speculation suggested that one of the rail buttons may have slight stuck to the guide rail. The propulsion system produced over 250 lbf. of thrust at launch, which would easily overcome any guidance resistance, but may have caused a small perturbation. Due to the large ballast weight added to the nose for static stability, the system performed analogous to an inverted pendulum that is slightly off balance. Thrust was no longer perfectly aligned between the C_g and vertical, causing the rocket to tilt. The excessively large fins performed excellent and maintained a nearly vertical ascent, despite fighting the tilt. Based on the telemetry shown in Figure 8.7, the tilt was approximately 8° from true, which resulted in a max altitude of 5,774 ft. The

deviation from target altitude was expected due to the reduced weight of the payload exchange. As shown in Figure 8.8, the recovery system worked as intended and the main parachute reduced descent almost exactly to the predicted descent shown in Figure 6.13. The data log for both the port and starboard sensors, showed nominal values for the first few minutes, and then became saturated. The initial data suggested that the sensors were working as intended while the rocket sat on the launch pad. The sudden change to saturated values of both sensors at precisely the same time suggested one of two scenarios. Either the rocket experienced skin friction of a magnitude that far exceeded predicted values, or the delicate sensors broke from acceleration in excess of 87 m/s^2 . The max velocity was within predicted range, so it was concluded that the sensors must have broken.

CHAPTER 10

CONCLUSION

The design space exploration was successful and a fully functional launch vehicle was created to carry subsonic aerodynamics research payloads. From the design space, key parameters were identified and individually evaluated in exhaustive trade studies, which resulted in the optimal design that experimentally satisfied the following mission requirements:

- Total impulse limit of 5,120 $N \cdot s$
Aerotech L1150R - 3,517 $N \cdot s$
- Minimum rail exit velocity of 52 ft/sec
Raid exit of 74 ft/sec @ 12 ft.
- Minimum static stability of 2.0
Static stability of 6.12
- Max velocity < Mach 1.0 Max
velocity of Mach 0.62
- Electronically track each section
Telemetry included GPS data

Of the six mission requirements, two were unable to be fulfilled. The kinetic landing requirement was 150 ft-lbf and experimental data showed 157.43 ft-lbf. The increased kinetic energy was a result of the extra mass added as ballast for stability.

Due to motor availability, the target altitude of one mile was not reached, but computer simulation was able to predict the sub-scale test flight data to within 1%. The computer model predicted an apogee of 6,068 ft., where the experimental data was 6,020 ft. Low cost prototyping helped to identify areas of weakness, such as faulty recovery wiring, that once fixed, allowed for a successful maiden flight of the full-scale vehicle. Although neither payload was successful, future SJSU students have a proven launch vehicle to fly new payload designs.

CHAPTER 11

FUTURE WORK

As the launch vehicle performed as expected, most of the future improvements should be focused on the research payloads, with one exception. A variable ballast system could be designed and situated closer to the C_g , to avoid the inverted pendulum problem in the future. The disadvantage to placing the ballast towards the center of the rocket, is more weight is needed to shift the C_g . This would be of little concern if altitude is not one of the mission requirements, as long as a sufficient motor is available to ensure safe rail exit velocity.

Since the strain gauges broke, a more robust sensor package could be designed. Either acquire strain gauges that are less delicate, or find a better way to protect them. Gluing the entire strain gauge lead to the airframe, was not sufficient to prevent it from breaking. As an alternative to strain gauges, the pitot tube system could be reevaluated. Even though these are less delicate than strain gauges, high subsonic flow still presents a risk of damage, which needs to be mitigated.

REFERENCES

- [1] National Aeronautics and Space Administration, 2017 NASA Student Launch Handbook: Colleges and Universities (NP-2016-08-101-MSFC), 2016.
- [2] Treichel, T., Telemetry and GPS Techniques for High Powered Rocket Recovery, *42nd International Conference on Environmental Systems*, International Conference on Environmental Systems (ICES), San Diego, California, USA, 15-19 July 2012.
- [3] Weir, A., *The Martian: A Novel*, 2011.
- [4] Madden, R.B., A Statistical Analysis of the Roll Rate of a Launch Vehicle under the Influence of Random Fin Misalignments, *AIAA Journal*, Vol. 10, No. 3, 1972.
- [5] Behr, V., Cole, J., Croll, R., The development of a ram air decelerator for the recovery of artillery shells, *11th Aerodynamic Decelerator Systems Technology Conference*, Aerodynamic Decelerator Systems Technology Conferences, San Diego, California, USA, 9-11 April 1991.
- [6] Levin, D., Shpund, Z., Deployable conical stabilizer and decelerator, *13th Aerodynamic Decelerator Systems Technology Conference*, Aerodynamic Decelerator Systems Technology Conferences, Clearwater Beach, Florida, USA, 15-18 May 1995.
- [7] Nose Cone Design, Wikipedia, URL:
<https://en.wikipedia.org/wiki/Nose_cone_design>, retrieved 1 Jun 2017.

APPENDIX A

ARDUINO CODE

```
#include <SD.h>
#include <SPI.h>

//Declare variables
float port; //port side sensor
float starboard; //starboard side sensor

unsigned long milli;
unsigned long sec;
int wait = 100; //wait for 1/10th of a second

//Create strain data file for SD
File strainData;

void setup() {
  Serial.begin(9600);

  pinMode(10, OUTPUT);
  digitalWrite(10, HIGH);

  Serial.print("Initializing SD card...");

  if (!SD.begin(10)) {
    Serial.println("initialization failed!");
    return;
  }
  Serial.println("initialization done.");
}

void loop() {

  //For debugging purposes **can comment out during actual use**
  Serial.print("Time: ");
  Serial.println(sec);
  Serial.print("  Fore: ");
  Serial.println(port);
  Serial.print("  Aft: ");
  Serial.println(starboard);

  //Record data to SD card
  File strainData=SD.open("data.txt", FILE_WRITE);
  if (!strainData){
    Serial.print("file didn't open");
```

```
}

//Get analog values
port = analogRead(A14);
starboard = analogRead(A15);

//Determine timestamps for easy SD card analysis
milli = float(millis());
sec = float(milli/1000);

strainData.print("Time: ");
strainData.println(String(sec));
strainData.print(" Port: ");
strainData.println(String(port));
strainData.print(" Starboard: ");
strainData.println(String(starboard));
strainData.close();

//Arduino delay 'wait' integer value before recording next data point
delay(wait);
}
```

APPENDIX B

ADDITIONAL SCHEMATICS

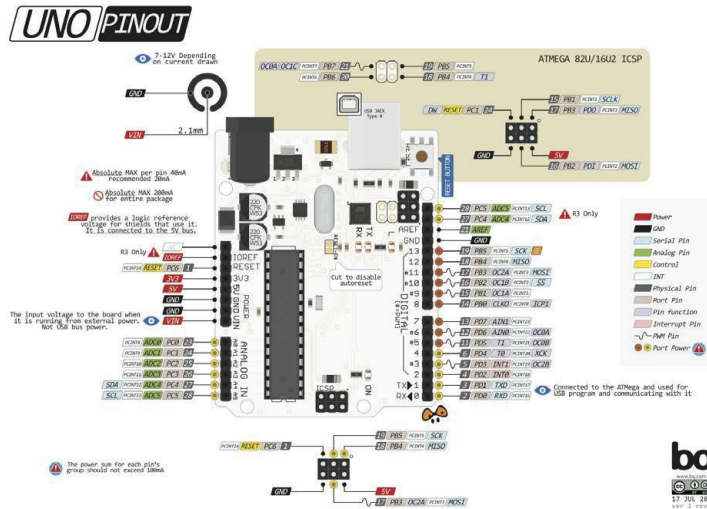


Figure B.1: Arduino Uno schematic

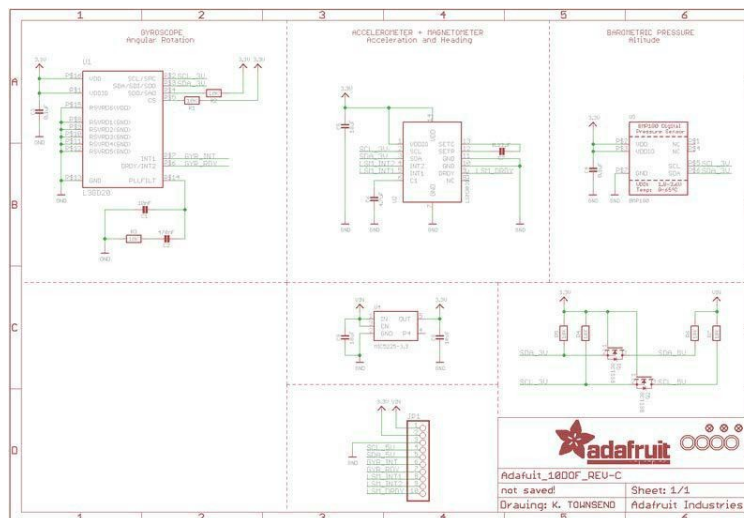


Figure B.2: Adafruit 10 DOF IMU schematic

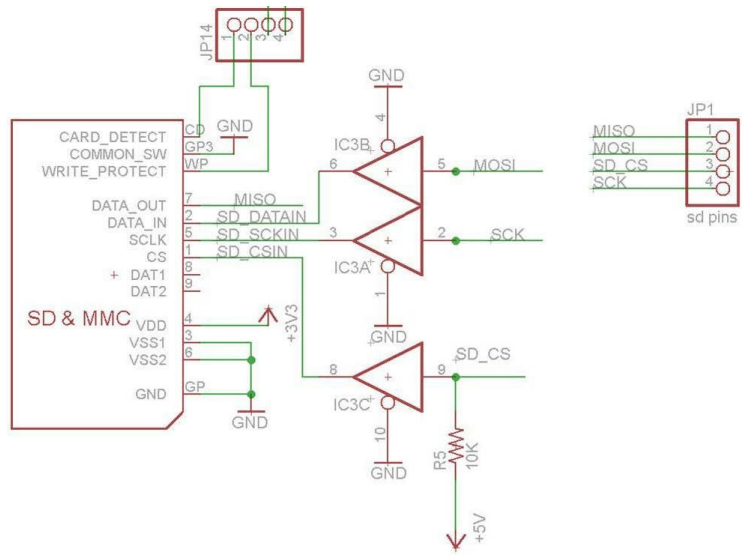


Figure B.3: Adafruit SD reader schematic

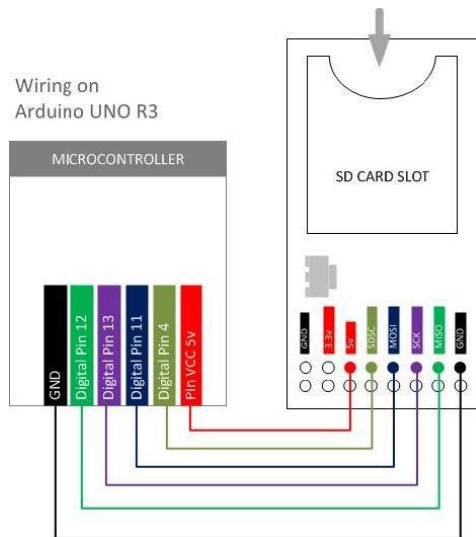


Figure B.4: Arduino to SD reader wiring